Water Resources Research

RESEARCH ARTICLE

Key Points:
- A novel algorithm for estimating reservoir storage from satellite remote sensing
- Storage time series for 21 reservoirs in South Asia from 2000 to 2012
- Data products were validated by gauge observations

Correspondence to:
H. Gao,
hgao@civil.tamu.edu

Monitoring reservoir storage in South Asia from multisatellite remote sensing

Shuai Zhang[1], Huilin Gao[1], and Bibi S. Naz[2]

[1]Zachry Department of Civil Engineering, Texas A&M University, College Station, Texas, USA, [2]Oak Ridge National Laboratory, Oak Ridge, Tennessee, USA

Abstract Reservoir storage information is essential for accurate flood monitoring and prediction. South Asia, however, is dominated by international river basins where communications among neighboring countries about reservoir storage and management are extremely limited. A suite of satellite observations were combined to achieve high-quality estimation of reservoir storage and storage variations in South Asia from 2000 to 2012. The approach used water surface area estimations from the Moderate Resolution Imaging Spectroradiometer (MODIS) vegetation indices product and the area-elevation relationship to estimate reservoir storage. The surface elevation measurements were from the Geoscience Laser Altimeter System (GLAS) on board the Ice, Cloud, and land Elevation Satellite (ICESat). In order to improve the accuracy of water surface area estimations for relatively small reservoirs, a novel classification algorithm was developed. In this study, storage information was retrieved for a total of 21 reservoirs, which represents 28% of the integrated reservoir capacity in South Asia. The satellite-based reservoir elevation and storage were validated by gauge observations over five reservoirs. The storage estimates were highly correlated with observations (i.e., coefficients of determination larger than 0.9), with normalized root mean square error (NRMSE) ranging from 9.51% to 25.20%. Uncertainty analysis was also conducted for the remotely sensed storage estimations. For the parameterization uncertainty associated with surface area retrieval, the storage mean relative error was 3.90%. With regard to the uncertainty introduced by ICESat/GLAS elevation measurements, the storage mean relative error was 0.67%.

1. Introduction

More than 45% of the global land area (excluding Greenland and Antarctica) is covered by a total of 261 international river basins [*Wolf et al.*, 1999]. The hydrologic and political effects of transboundary rivers are enormous. Across the world, South Asia is the region that suffers the most from these impacts. Throughout much of history, certain transboundary rivers such as the Ganges, Indus, and Brahmaputra rivers have served as the cultural and economic backbone of South Asia, which contains one of the largest and densest populations in the world. However, these transboundary rivers, along with the reservoirs on the rivers, are a near-constant source of conflict between countries in the region. Due to these social, economic, and politically induced conflicts, countries in this region have largely failed to reach any agreements on sharing the waters of these transboundary rivers [*Biancamaria et al.*, 2011]. Consequently, the lack of communication, particularly about reservoir storage and management, exacerbates the casualties and economic losses from flood events. Statistics based on past records show that South Asia experiences one of the highest fatality rates in the world due to floods [*Adhikari et al.*, 2010]. Therefore, there is a strong societal need to advance the scientific understanding of the flood regimes in South Asia and provide decision makers with the information needed to better manage the reservoirs.

Satellite remote sensing has offered a unique opportunity to study the Earth from space [*Rodrigues et al.*, 2012]. Its global coverage (which is free of geographical and political limitations) has shed light on flood monitoring and forecasting in these international river basins. One of the applications is to force hydrological models with satellite precipitation products (e.g., the Tropical Rainfall Measurement Mission (TRMM) product) to estimate river discharges [*Huffman et al.*, 2007]. However, because reservoirs have not been implemented in hydrological models in an operational fashion at large scale, a direct result is a significant number of false alarms in basins with large reservoirs [*Wu et al.*, 2012]. Therefore, near-real-time observation data showing water storage for the reservoirs over these international basins is essential for improving

hydrological modeling forecast skills and mitigating flood costs effectively. Even in cases when there is a time lag with the observation data, the model results can still be enhanced through techniques such as data assimilation [*Bulygina and Gupta*, 2011; *Zaitchik et al.*, 2008].

The common approach for monitoring reservoir storage using remote sensing data is to retrieve water surface area and elevation separately, and then combine these two pieces of information for calculating the storage [*Cretaux et al.*, 2011; *Gao et al.*, 2012]. For measuring surface water extent, the most commonly used spaceborne instruments are the Thematic Mapper (TM)/Enhanced Thematic Mapper Plus (ETM+) onboard Landsat, and the Moderate-Resolution Imaging Spectroradiometer (MODIS) onboard Earth Observation System (EOS) Terra and Aqua satellites. Landsat has a high spatial resolution of 30 m with a repeat cycle of 16 days. Despite the benefits of its high spatial resolution, its low temporal resolution hampers its monitoring capability—especially when the images are impacted by cloud contamination. For instance, *Mercury et al.* [2012] found that on average Landsat views are 48% cloud free between 60°N and 60°S over land. Compared to Landsat, MODIS has a much higher temporal resolution (i.e., daily). The trade-offs of MODIS sensors are the coarser spatial resolutions (250 m/500 m/1000 m), along with the larger viewing angles ($\pm 55°$). Nevertheless, the 16 day composite of MODIS images has a much larger cloud-free coverage area than that of the (once every 16 days) Landsat image. This advanced temporal resolution is critical for monitoring purposes.

For estimating water surface area, index-threshold-based approaches and image classification-based approaches are most commonly used [*Cheema and Bastiaanssen*, 2010; *Dewidar*, 2011; *Lu et al.*, 2011; *Wu and Liu*, 2014]. Index-threshold-based approaches have the advantage of estimating the water surface area with little computation. For example, the Normalized Difference Vegetation Index (NDVI) value of a water pixel is either negative or close to zero. Therefore, a threshold (e.g., zero) can be set to differentiate the water and nonwater pixels on remote sensing images [*Islam et al.*, 2010]. In vegetated areas with abiotic lakes, this might work rather well given the large NDVI contrast. However, separation of water from barren areas of rock, sand, or snow will cause difficulties as these surfaces correspond to NDVI values close to zero (-0.1 to 0.1). Similarly algae blooms would cause significant trouble by exceeding the chosen threshold. Therefore, other indices, such as the modified normalized difference water index (MNDWI) [*Xu*, 2006] have also been used for extracting water coverage. Nonetheless, because both atmospheric absorption and water quality vary by lake location, more accurate extraction of water bodies requires the threshold to be manually adjusted according to actual situations [*Ji et al.*, 2009]. When multiple reservoirs are studied simultaneously on a large scale over a long period, the work load for adjusting the threshold will increase since each reservoir needs to be treated separately. Meanwhile, the accuracy of these results will decrease as it is hard to apply one threshold to all of the varying situations—even just for one reservoir. To avoid this problem, unsupervised image classification algorithms, which minimize human error, are preferred for extracting water surface area [*Cheema and Bastiaanssen*, 2010; *Lu et al.*, 2011]. Despite their advantages of classifying water coherently (for each reservoir image) at a large scale, unsupervised algorithms—which work by minimizing the intracluster (i.e., within a given cluster) sum of squares—sometimes can be trapped in local optima, and the accuracy of classification results can be compromised [*Maulik and Saha*, 2010]. In order to improve the accuracy for water surface estimation, *Gao et al.* [2012] developed a new method which combines the index and classification algorithms. A classification mask was derived based on the percentile image of a set of crude classifications (using 0.1 as the NDVI threshold). The *k*-means classification algorithm [*Duda et al.*, 2001; *Jain*, 2010], which aims at minimizing the variance within a cluster, was applied to each NDVI image within the masked area. The *Gao et al.* [2012] algorithm is the first validated algorithm that has been used for estimating surface area of globally distributed reservoirs from one single sensor. This is essential for the consistency of the reservoir product, both in terms of error analysis and uncertainty quantification.

Besides the surface area, water surface elevation is also needed for estimating reservoir storage. Satellite radar altimetry has been the most commonly used data source for estimating surface elevations of water bodies [*Calmant et al.*, 2008]. There are several databases which provide elevation data from ENVISAT, GFO, Jason-1, Jason-2, and Topex/Poseidon (T/P) satellites [*Birkett and Beckley*, 2010; *Crétaux et al.*, 2011; *McKellip et al.*, 2004]. However, due to the coarse cross-track spacing (several hundred kilometers) and the relatively stretched along-track path length required to obtain accurate vertical measurements (typically 10 km or so), such elevation data are only available for a couple hundred large lakes and reservoirs. The root mean square

errors of radar altimeters range from about 3 to 33 cm, depending on the size of the target and the sensors [*Birkett*, 1998; *Birkett and Beckley*, 2010]. In addition to the radar altimeters, the Geoscience Laser Altimeter System (GLAS) onboard the Ice, Cloud, and land Elevation Satellite (ICESat) has been used for measuring lake/reservoir elevations. Compared to radar altimeters, ICESat/GLAS has a high horizontal spatial resolution (approximately 70 m) and a high vertical precision (about 10 cm) [*Zhang et al.*, 2011]. These advantages allow ICESat/GLAS to detect elevations for much smaller water bodies (with higher accuracy) than a typical radar altimeter can. However, the use of ICESat/GLAS for monitoring water elevations operationally has been hindered by its short lifetime and long repeat period (91 days). During its lifetime from 2003 to 2010, the ICESat/GLAS instrument only collected elevations during designated campaigns [*Wang et al.*, 2013]. As a result, most of the lake studies using the ICESat/GLAS focus on interannual elevation variations [*Li et al.*, 2011; *Phan et al.*, 2012; *Shuman et al.*, 2006; *Wang et al.*, 2013; *Zhang et al.*, 2011].

Although a number of studies have used satellite data to estimate reservoir storage, the existing algorithms are all limited in different ways. For instance, in methods based on Landsat images and ICESat/GLAS data [*Duan and Bastiaanssen*, 2013; *Song et al.*, 2013], the empirical relationship between the ICESat/GLAS elevation and the Landsat water surface area was established so that storage can be estimated by area when the ICESat/GLAS data were unavailable. However, the number of days when reservoir volume can be estimated is still very low because the Landsat repeats every 16 days, and its images often suffer from cloud contamination. Most of the more frequent storage observations rely on elevations from radar altimeters. *Crétaux et al.* [2011] had combined such elevations with area estimations from various sources (e.g., Landsat, CBERS-2, ASAR). Due to the variety of sensor spatial/temporal resolutions and frequencies, there is a lack of consistency within the product, and the product uncertainties are hard to quantify. In contrast, *Gao et al.* [2012] developed a global large reservoirs storage estimation algorithm which only relies on the MODIS NDVI product for estimating surface areas. The trade-off of using the medium resolution MODIS data (250 m) is that fractional water coverage for the MODIS pixels at the reservoir borders introduces error during the unsupervised classification, which especially lowers the accuracy for reservoirs with complicated shorelines. In summary, simultaneously optimizing both the spatial/temporal resolution and the coverage remains the biggest challenge toward monitoring more reservoirs with high accuracy.

In South Asia, despite the significant benefits that would result from having near-real-time reservoir storage information, this has been difficult to obtain because remotely sensed surface elevation values from radar altimeters are only available for a few large reservoirs sporadically. Although water surface elevation through ICESat/GLAS is an alternative, to our knowledge, there has been no storage estimations available over South Asia based on this data source. The objective of this paper is to generate a validated remotely sensed reservoir storage data set in the South Asia region which can be used for various water resources management and Earth System Modeling applications. For this purpose, the *Gao et al.* [2012] MODIS area algorithm was improved such that high-quality water storage estimations can be achieved using ICESat/GLAS elevation and MODIS surface area. In addition to the data analysis and results validation, storage estimation uncertainties (due to reservoir surface area retrieval algorithm parameterization and elevation measurement errors) were also quantified.

2. Data Sources and Reservoir Selection

This section describes the data sources and the criteria used for selecting the reservoirs monitored in this study.

2.1. Satellite Data
2.1.1. MODIS Data
The MODIS data, which were used for estimating reservoir area, are available from the NASA Land Processes Active Archive Center (http://lpdaac.usgs.gov/). Specifically, we acquired the NDVI 16 day product at 250 m spatial resolution as a gridded level-3 product in Sinusoidal projection (MOD13Q1) [*Solano et al.*, 2010] from Terra. The latency of the product ranges from zero to 16 days, depending on the difference between the last product release date and the current date. The reasons for choosing MOD13Q1 are: (1) its 250 m spatial resolution is highest among the MODIS products, and (2) Terra MODIS products became available in February 2000, while the counterpart Aqua MODIS products were not available until July 2002

2.1.2. ICESat/GLAS
The ICESat mission was launched in January 2003 and it ended in February 2010 [*Shuman et al.*, 2006; *Zhang et al.*, 2011]. The GLAS on ICESat provides global measurements of polar ice sheet mass balance, cloud and

aerosol heights, land topography, and vegetation characteristics with unprecedented accuracy [*Schutz et al.*, 2005; *Zhang et al.*, 2011; *Zwally et al.*, 2002]. The ICESat/GLAS Release-33 elevation data available from 2003 to 2010 were obtained through the U.S. National Snow and Ice Data Center (NSIDC, http://nsidc.org/data/icesat/). During the two mission validation periods (20 February 2003 to 21 March 2003 and 25 September 2003 to 4 October 2003), the ICESat/GLAS repeat time was 8 days. However, during the rest of the mission, its repeat time was 91 days. A given location along the tracks of ICESat/GLAS was typically observed less than 24 times during the entire mission period with a vertical precision of better than 10 cm [*Zhang et al.*, 2011; *Zwally et al.*, 2008].

2.1.3. Landsat 7 Enhanced Thematic Mapper Plus (ETM+)

To evaluate MODIS-based water area estimations, Landsat 7 ETM+ Level 1 data were employed to create high-quality water classification images. For each of the five selected reservoirs (section 2.3), a Landsat 7 ETM+ image with little cloud contamination (less than 10%) was acquired from the USGS website (http://earthexplorer.usgs.gov/). The Support Vector Machine (SVM) supervised classification approach [*Boser et al.*, 1992; *Cortes and Vapnik*, 1995] was then used to generate the corresponding Landsat water classification image from bands 1–5 and 7.

2.2. Gauge Observations

For validating the remotely sensed reservoir elevation and storage estimations, gauge observations reported by the Indian Century Electricity Authority (CEA) were employed. The online data set (which is available at http://www.cea.nic.in/hyd_arch.html) contains daily reservoir elevation, storage, and cumulative energy generation data for 30 hydropower reservoirs from 2008 to present, with a lag time of about 2–4 months.

2.3. Reservoir Selection

Reservoir information provided by the Global Reservoir and Dam (GRanD) database [*Lehner et al.*, 2011] was utilized to help identify the reservoirs selected in this study. Considering the medium resolution of MODIS NDVI and the narrow ICESat/GLAS tracks, the GRanD reservoirs which meet the following criteria were selected: (1) the area at capacity is larger than 65 km^2—which is equivalent to a total of 1040 MODIS NDVI grid cells (at 250 m $\times$ 250 m each)—to ensure that it (the surface area) can accurately be estimated from the medium resolution MODIS NDVI (250 m); and (2) there were at least five along-track ICESat/GLAS water surface elevation measurements (each with a footprint of 70 m and along track spacing of 172m) over the selected reservoir for each overpass (such that an average elevation—which represents the entire reservoir—can be paired up with the MODIS area).

Following the above criteria, a total of 21 reservoirs were chosen for this study, which represent 28% of the integrated reservoir capacity in South Asia (according to the GRanD database). The locations of these reservoirs are shown in Figure 1.
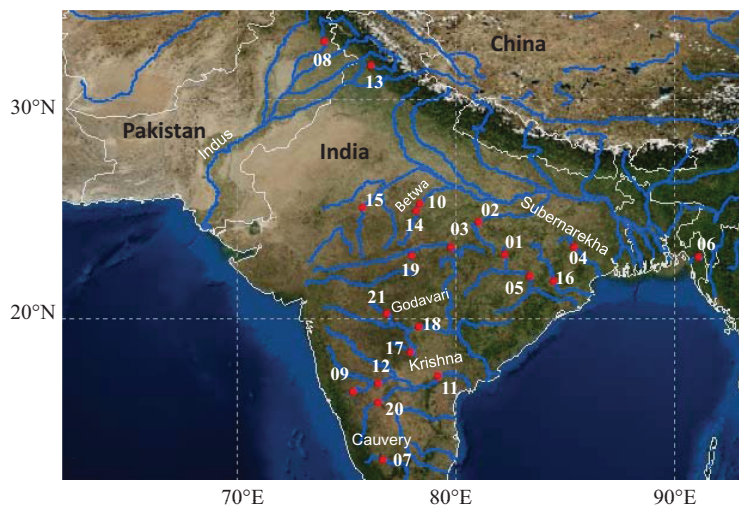
Figure 1. Locations of 21 selected reservoirs in South Asia. For each reservoir ID, detailed information (e.g., name, location, capacity) is provided in Table 1.

3. Methodology

The algorithm for estimating the reservoir storage contains the following steps: (1) estimation of the water surface area of reservoirs based on MODIS NDVI images from 2000 to 2012; (2) extraction of the reservoir surface elevations from ICESat/GLAS data; (3) establishment of the area-elevation relationship for the reservoir of interest, and then retrieving the water surface elevation value from the water surface area value using the established relationship; and (4) calculation of the reservoir storage over time from water surface elevation and area time series. Figure 2 shows the flowchart of the algorithm. More details of the algorithm are described in the following paragraphs.

3.1. Surface Area Estimation

The surface area estimation method is a modification of the algorithm created by *Gao et al.* [2012]. In *Gao et al.* [2012], the storage estimations based on MODIS surface areas (using the area-elevation relationship) were not as good as the storage estimations based on radar altimeter elevations. Given the goal of this study is to use MODIS surface area (considering the limited availability of ICESat/GLAS elevation observations) as the primary input for estimating storage, it is essential to improve upon the earlier [*Gao et al.*, 2012] MODIS area algorithm. Therefore, a classification enhancement approach was developed for this study. The main idea is to enhance individual scenes based on the percentile information from the 13 year water probability reference data to correct misclassified pixels, and to assign an appropriate class to the unclassified pixels. The basic principle is to use the spatial and temporal information from the NDVI images along with the fact that inner parts of the reservoir are more likely to be classified as water (as compared to outer parts). This approach helps enhance the area retrieval accuracy and facilitate successful retrieval—even in the case when a large portion of an image is of low data quality (e.g., cloud contaminations). Here we explain the updated algorithm entirely using the following steps (as illustrated in Figure 2).

1. Mask creation. For each 16 day NDVI image from 2000 to 2012 (296 images in total), an index-threshold-based approach was used—such that pixels with NDVI values less than 0.1 were considered as water. As a result, 296 water coverage images were created. A water coverage percentile image (herein after referred to as a mask) was then calculated with every pixel value representing the percentage of that pixel had been counted as water (in the 296 water coverage images over the 13 year period). Then, an extension was generated by expanding the mask to a buffer area which covered any "nonwater" areas that fell within a (3 × 3 pixels) moving window centered on each water pixel. This way the mask and its buffer area would be able to cover all possible water pixels for the studied reservoir. Figure 3 shows an example of the extended mask (with its buffer area included) over the Hirakud reservoir.

2. *k*-means classification. The *k*-means clustering algorithm was applied to classify all pixels of the MODIS NDVI image within the extended mask area. The pixels were divided into three classes: "water," "nonwater dry surface," and "nonwater wet surfa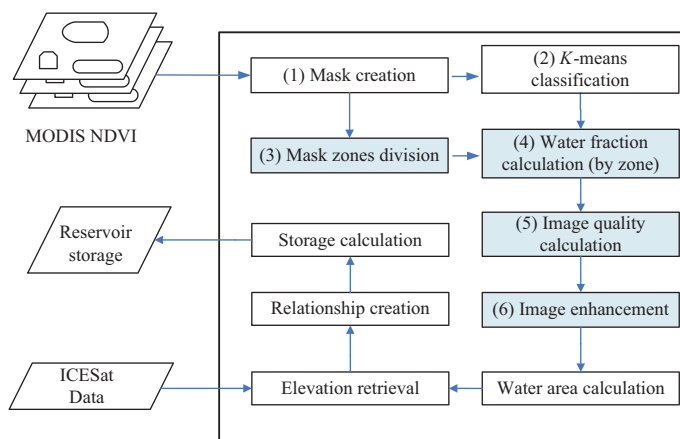ce." The classification within the extended mask area alone can effectively reduce the amount of computation and increase the accuracy of MODIS water area estimation (relative to not using a mask as a constraint). However, the accuracy of this classification approach also depends on the quality of the MODIS NDVI data and the purity of pixels. In order to solve the problems caused by pixels with bad quality, the following screening process was used: if the reliability of a pixel was not denoted as "good data" (i.e., the pixel was identified as "cloudy," or "snow/ice,"

Figure 2. Flowchart of the reservoir storage estimation algorithm, with the image enhancement process highlighted in blue.
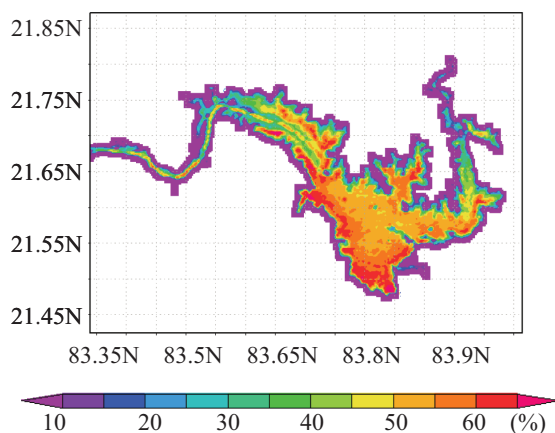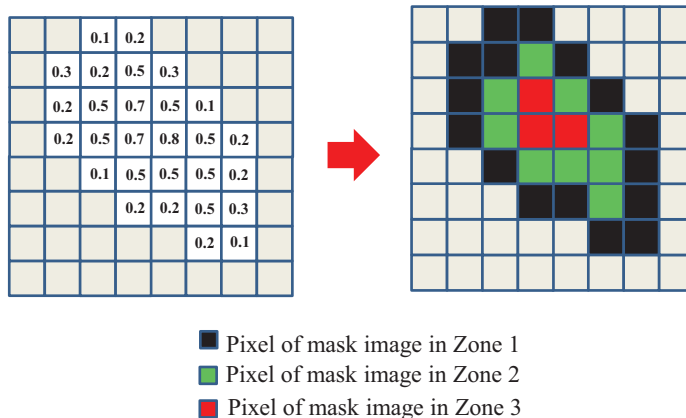
Figure 3. Mask of the Hirakud reservoir (with percentile for water class). Note a pixel (from a MODIS NDVI image) is considered to be covered by water when NDVI < 0.1. Percentile is calculated for that pixel from 296 water coverage images from 2000 to 2012.

or "marginal"), then it was designated as "unclassified" (i.e., neither "water" nor "nonwater"). *Gao et al.* [2012] used a majority filter as a post classification processing mechanism to eliminate the "salt and pepper" effect [*Al-amri et al.*, 2010; *Gonzalez and Woods*, 2007]. Nonetheless, this filtering does not improve the accuracy much when the low-quality MODIS NDVI pixels cover a large portion of the image. The pixel purity problem, which is caused by a mixture of surface components within a pixel, is much less a concern. This is because the purity problem only occurs within the boundary pixels, and the errors (overestimation/underestimation) usually cancel out (unless the NDVI values for the nonwater portion have a very large annual variation) [*Gao et al.*, 2012].

3. Mask zones division. The mask image (without the buffer area) was grouped into 50 zones based on the percentile information, using a fixed increment percentile value of 2%. This threshold (of 2%) allowed us to narrow down the differences among pixels within a given zone. In other words, all the pixels within the same zone indicate that they have a similar possibility of being classified as water. Here we use a simple synthetic example (with only three zones) to explain the concept and process. In the example, the mask image contains 8 × 8 pixels with the percentile values as shown in Figure 4. Using a threshold of 1/3 (which is one divided by the number of zones), the mask area can be divided into three different zones. Each pixel in the mask image is then assigned to a zone (zone 1, 2, or 3) according to its percentile value. For instance, since the two pixels in the top row of Figure 4 have the percentiles of 0.1 and 0.2 (which are both between 0 and 1/3), they are each assigned to zone 1.

4. Water fraction calculation (by zone). Zonal water coverage maps are created for each classification image by overlaying the percentile mask image on it (shown in Figures 5a and 5b). The percentage of water pixels within each zone is calculated using equation (1):

$$p_i = \frac{n_i}{N_i}, \quad i = 1, 2, \ldots, K \tag{1}$$

where n_i is the number of pixels in the i_{th} zone that are classified as water (according to the MODIS NDVI threshold), N_i is the total number of pixels in the i_{th} zone (according to the delineation of the mask image), and K is the total number of zones. In the simple synthetic example, the p_i value for zone 1, zone 2, and zone 3 are 15/16, 6/9, and 0/3, respectively.

5. Image quality assessment. A quality parameter (Q) is computed for each classification image according to equation (2).

$$Q = \frac{\sum_{i=1}^{K} (p_i - 0.5)^2}{K} \tag{2}$$

Q is a measure of the overall consistency of the surface water classification from a MODIS NDVI image. Given p_i is from 0 to 1, Q has a range between 0 and 0.25. The Q value increases as the quality of a water classification image increases. If a classification is of
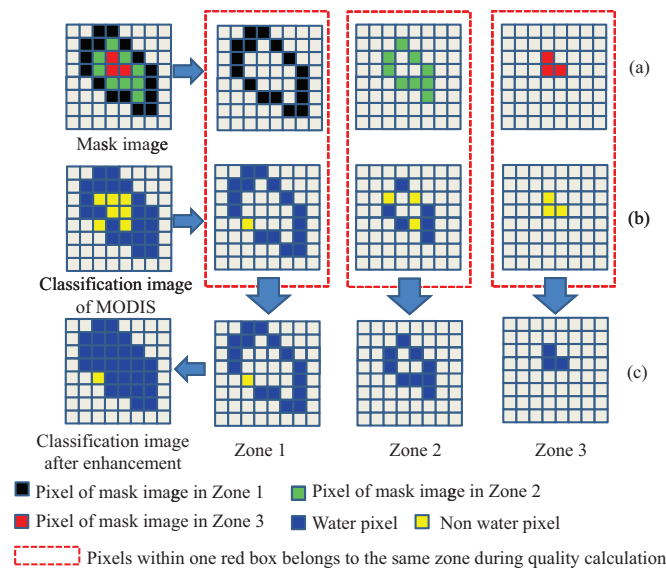
Figure 4. A simple example of dividing the mask into different zones according to its percentile values (Zone 1: 0–0.33, Zone 2: 0.33–0.66, and Zone 3: 0.66–1).

Figure 5. A simple example showing the classification image enhancement process: (a) dividing the mask file into multiple zones; (b) assigning zone values to the classified image; and (c) enhancing the classified image based on image quality.

high quality, then the p_i values for the zones classified as water should be 1 (or close to 1), while the p_i values for the zones classified as land should be zero (or close to zero). In the case of an ideal classification (i.e., p_i equal or close to 1 or 0 for all i values), the Q value is close to the maximum (0.25). In contrast, if a classification image is of very low quality, the p_i values for most of the zones should be close to 0.5 (0.5 represents the case of a random distribution of water pixels within a zone). As a result, the Q value is close to zero for a low-quality image. For the sample classification illustrated in Figure 5, its Q value equals to 0.156.

6. Classification image enhancement. For each zone ($i = 1, 2, \ldots, K$) within one classification image, if its p_i value is larger than a threshold T, then all pixels in the next zone (i.e., j_{th} zone, j ranges from $i+1$ to K) are set as water. The threshold T is determined according to equation (3):

$$T = \begin{cases} C_p & Q > C_Q \\ p_m & Q \leq C_Q \end{cases} \qquad (3)$$

where p_m is the median of all the p_i values within one classification image, and C_p and C_Q are both constant parameters. The threshold value T for each image is based on its quality Q: if Q is larger than C_Q, then T is equal to C_p; otherwise, T equals p_m. Calibrated over two reservoirs where observations are available (i.e., the Pong and Hirakud reservoirs), C_p and C_Q are set to 0.7 and 0.1, respectively. The uncertainties associated with these parameter selections are discussed further in section 4.2.1. The enhancement process for this simplified example is illustrated in Figure 5c. Given that the Q value ($Q = 0.156$) of the classification image is larger than C_Q ($C_Q = 0.1$), the threshold T is set to 0.7. For this classification image, since p_1 ($p_1 = 0.94$) is larger than T ($T = 0.7$), all pixels in zone 2 and zone 3 are assigned as water.
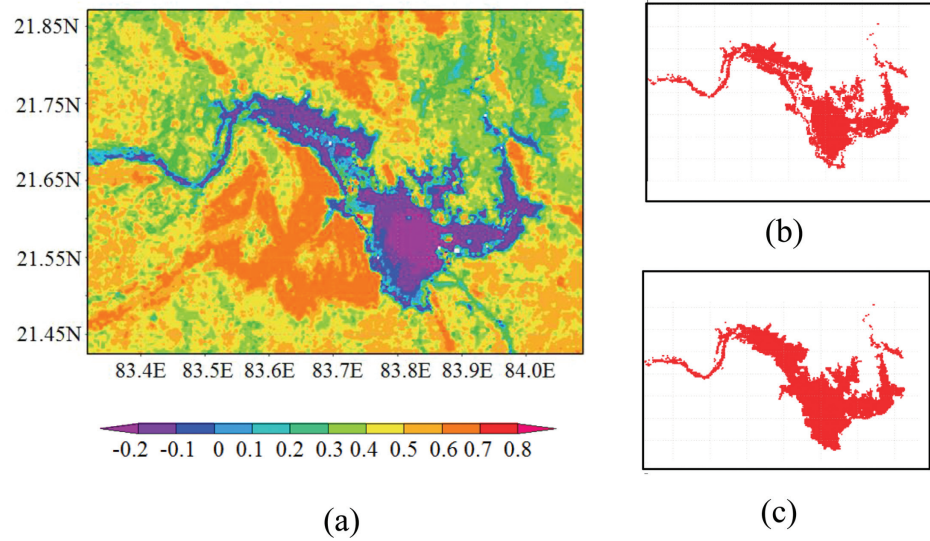
This classification image enhancement is based on two principles. First, a good classification image should have good consistency—meaning pixels in the same zone should have the same classification results. Second, pixels in the zones with a higher percentile should have a greater possibility of being classified as water than those in zones with lower percentile values. This means that if the probability that a zone is covered by water exceeds the threshold T (as defined in equation (3)), all pixels of the remaining inner lake zones are also labeled as water. As an example, the water classification results for the Hirakud Reservoir (day 305 of 2011) are shown in Figure 6. The quality parameter Q for Figure 6b is 0.080, and the threshold T is equal to p_m ($p_m = 0.64$). By comparing the T value (i.e., 0.64) with the p_i values by zone, the initial classification image (i.e., Figure 6b) was enhanced by assigning all pixels from zone 15 to zone 50 as water (as shown in Figure 6c). The classification improvement due to the enhancement operation can be detected by visually comparing Figures 6b and 6c.

After the preliminary classification and image enhancement are completed, the reservoir surface area can be estimated by summing up all the water pixels within the classification image (as the area for each MOD13Q1 pixel is a constant 0.25×0.25 km^2). As an example, the water surface area time series for the Hirakud reservoir is shown in Figure 7a.

3.2. Water Surface Elevation Estimation From ICESat/GLAS
The reservoir surface elevation results were retrieved from ICESat/GLAS orbital measurements in two steps. First, using the reservoir area boundary identified by the MODIS water classification (that was closest in

Figure 6. An example of the Hirakud Reservoir showing the MODIS NDVI classification of day 305 of 2011. (a) The original MODIS NDVI image; (b) the classification results without image enhancement; and (c) the classification results after image enhancement.

time with the ICESat/GLAS overpass) and the ICESat/GLAS orbital geographical location information, all elevation measurements within the reservoir were extracted. Then, the representative elevation of a reservoir for a given day was estimated as the average of all the measurements within the overpassing orbit.
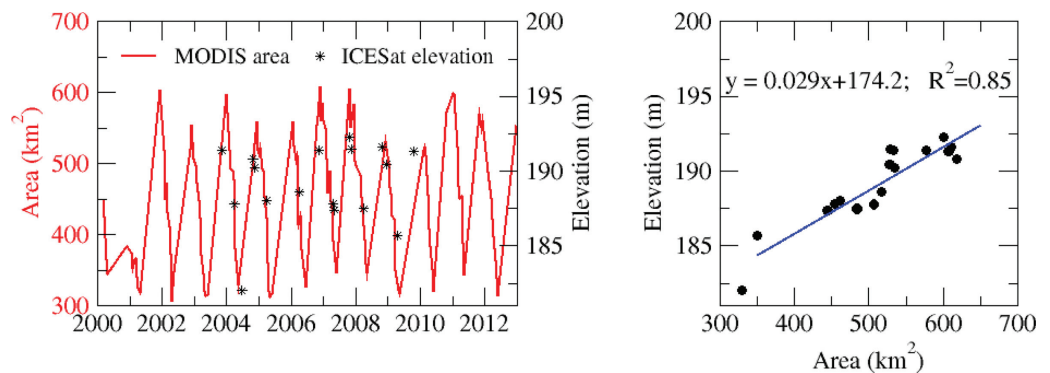
3.3. Area-Elevation Relationship
The water area and elevation data collected during the overlapping period were paired up for each reservoir to get reservoir-specific area-elevation relationships. Figure 7b shows one example of the area-elevation relationship for the Hirakud reservoir. By creating area-elevation relationships, we could use the MODIS-based water surface area to estimate the water surface elevation when the ICESat/GLAS data were not available. Table 1 shows the area-elevation relationships and coefficients of determination for all the reservoirs in this study.

3.4. Water Storage Estimation
Since the ICESat/GLAS elevation data were very limited, we could not combine the ICESat/GLAS water elevation and the MODIS water surface area directly to calculate the water storage. Instead, the elevation was inferred from the MODIS surface area and the area-elevation relationship. The storage was then estimated using equation (4):

$$V_{RS} = V_c - (h_c - h_{RS})(A_c + A_{RS})/2 \tag{4}$$

where V_c, h_c, and A_c represent storage, area, and water elevation at capacity, and V_{RS}, h_{RS} and A_{RS} are the estimated storage, area, and water elevation from remote sensing. Figure 8 shows the time series of reservoir storage for the Hirakud reservoir as an example.

Figure 7. The area-elevation relationship over the Hirakud reservoir (a) time series of MODIS surface water area and ICESat/GLAS surface elevation; (b) scatterplot for the area-elevation relationship.

Table 1. Reservoir Area-Elevation Relationships and Coefficients of Determination for the 21 Reservoirs

ID	Reservoir	Country	Location (°N, °E)	Area (km²)	Capacity (10^6 m³)	Purpose[a]	Area-Elevation Relationship[b]	R^2
01	Bango	India	22.61, 82.60	104	3416	I,E	y = 0.238x + 332.0	0.71
02	Bansagar	India	24.19, 81.29	384	5410	I,E	y = 0.051x + 318.6	0.98
03	Bargi	India	22.95, 79.93	268	3920	I,E	y = 0.101x + 398.9	0.96
04	Chandil	India	22.98, 86.02	174	1961	I,E	y = 0.14x + 171.4	0.77
05	Hirakud	India	21.52, 83.85	603	4709	I,E	y = 0.029x + 174.2	0.85
06	Karnafuli	Bangladesh	22.5, 92.23	777	6477	I,E,F	y = 0.073x + 13.67	0.81
07	Krisharaja Sagar	India	12.42, 76.57	100	1369	I,E,W	y = 0.277x + 729.2	0.88
08	Mangla	Pakistan	33.13, 73.64	251	7300	I,E,F	y = 0.243x + 311.7	0.64
09	Malaprabha	India	15.82, 75.09	130	1068	I,E	y = 0.112x + 612.6	0.96
10	Matatila	India	25.10, 78.37	139	1133	I,E	y = 0.112x + 297.7	0.90
11	Nagarjuna Sagar	India	16.57, 79.31	285	6538	I,E	y =0.379x + 100.2	0.90
12	Narayanapura	India	16.22, 76.35	102	1071	I	y = 0.140x + 478.6	0.77
13	Pong[c]	India	31.97, 75.95	260	6946	I,E	y = $0.237x^2$ − 188.6x + 37,675	0.96
14	Rajghat	India	24.76, 78.23	224	2172	I,E	y = 0.085x + 352.0	0.98
15	R. P. Sagar	India	24.92, 75.58	198	1568	I,E	y = 0.134x + 325.5	0.94
16	Rengali	India	21.28, 85.03	392	3168	I	y = 0.072x + 100.2	0.88
17	Singur	India	17.75, 77.93	105	850	W	y = 0.082x + 513.1	0.94
18	Sriram Sagar	India	18.97, 78.34	450	3172	I,E	y = 0.038x + 320.4	0.98
19	Tawa	India	22.56, 77.98	200	2310	I	y = 0.142x + 335.6	0.98
20	Tungabhadra	India	15.27, 76.33	390	3764	I,E	y = 0.05x + 481.1	0.75
21	Yeldari	India	19.72, 76.73	82	934.3	I,E	y = 0.459x + 41.6	0.98

[a]I is irrigation, E is electricity generation, W is water supply, and F is flood control.
[b]y is elevation and x is area.
[c]A quadratic area-elevation relationship was selected for Pong reservoir since its R^2 (0.96) is much higher than the R^2 from a linear relationship (0.89).

Using the methods explained in this section, time series values of reservoir surface area, surface elevation, and water storage were estimated for the 21 selected South Asian reservoirs from 2000 to 2012.
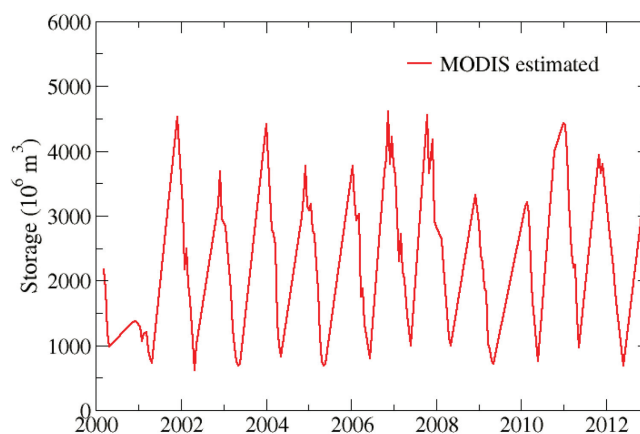
3.5. Statistical Criteria for Results Validation

Three statistical criteria were selected for validating the elevation and storage estimations from this study. They are the coefficients of determination (R^2, equation (5)), bias (B, equation (6)), and normalized root-mean square error (NRMSE, equation (7)).

$$R^2 = \frac{Cov(RS, Obs)}{D(RS)D(Obs)} \tag{5}$$

$$B = \overline{RS} - \overline{Obs} \tag{6}$$

$$NRMSE = \frac{\sqrt{\sum_{i=1}^{n} \frac{(RS_i - Obs_i)^2}{n}}}{\overline{Obs}} \tag{7}$$

where RS is the result from remote sensing, Obs is the observation data, n is the number of data points, and $\overline{RS}$ and $\overline{Obs}$ are the average values of the remote sensing result and the observational data. $Cov()$ means covariance and $D()$ represents the variance.

4. Results and Discussion

4.1. Results Validation

The remotely sensed results were validated comprehensively through two steps. First, the MODIS surface water classification

Figure 8. Time series of the MODIS-based storage estimations for the Hirakud reservoir.
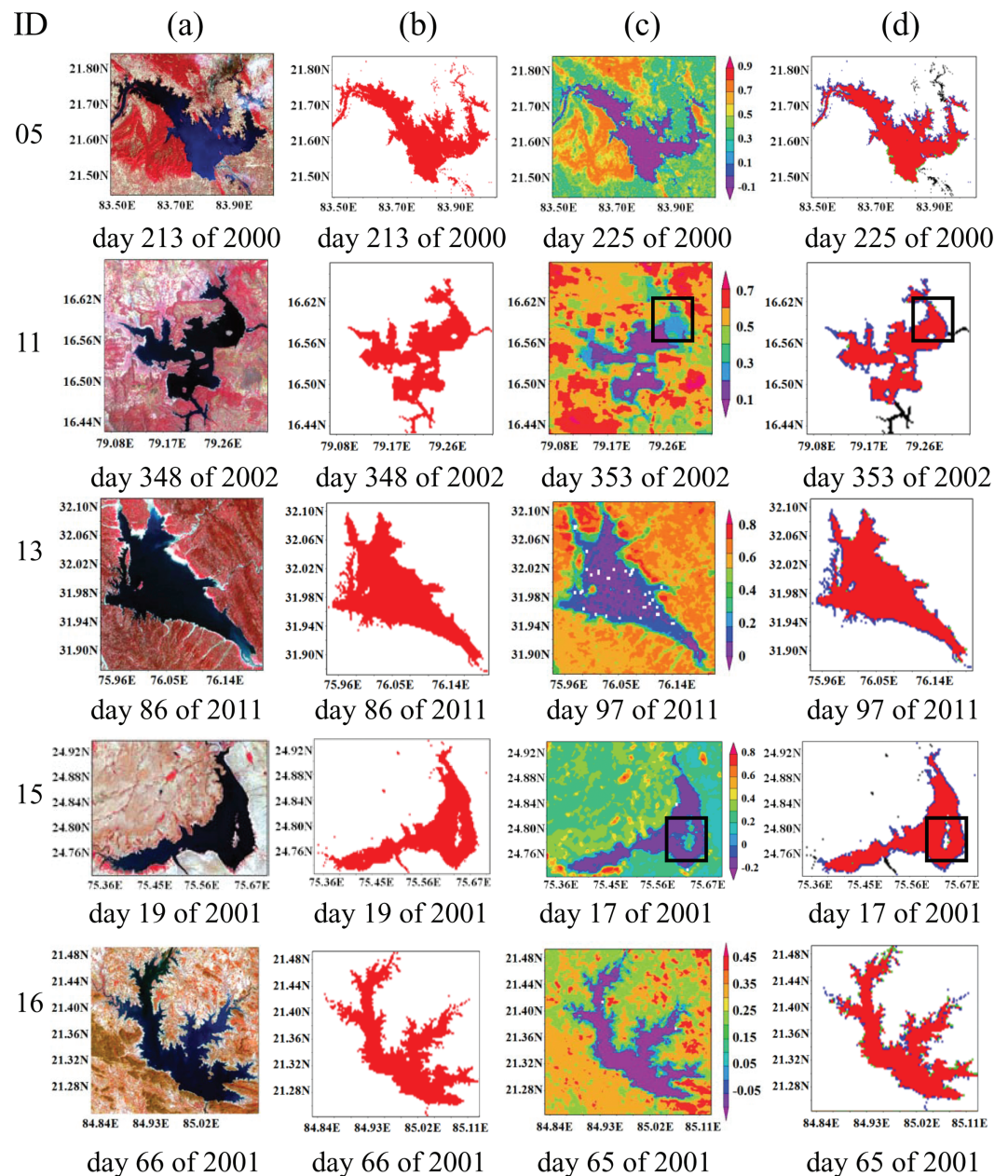
Figure 9. Comparisons between Landsat and MODIS surface water classification results: (a) Landsat ETM + images (RGB); (b) Landsat classifications; (c) MODIS NDVI images; (d) MODIS classifications over five reservoirs. The reservoirs are Hirakud (ID: 05), Nagarjuna Sagar (ID: 11), Pong (ID: 13), R. P. Sagar (ID: 15), and Rengali (ID: 16). Note that the date is the starting date of 16 day period. For Figure 9d, blue pixels stand for underestimated results, green pixels are overestimated results, and black ones are invalid classification pixels (such as a small lake outside the reservoir, or rivers connected with the reservoir). Black boxes (for some of the panels within Figure 9a and Figure 9d) are used to highlight the regions where the enhancement performed well.

images were compared with Landsat high-resolution (30 m) classifications. Second, the reservoir elevation and storage data set from remote sensing were evaluated with gauge observation. Five reservoirs (i.e., Rana Pratap Sagar, which is also referred to as R. P. Sagar; Hirakud; Nagarjuna Sagar; Pong; and Rengali) were selected for the validation, since they are the only ones among the 21 reservoirs with both observed elevation and storage data available (from 2008 to 2012).

Figure 9 shows the original Landsat false color images, Landsat classifications, MODIS NDVI images (which overlapped with the Landsat date), and MODIS classifications. The area estimations are summarized in Table 2. The MODIS classifications are in good agreement with the Landsat results, with percent error values ranging from 1% to 9%. The main differences are attributed to the different spatial resolutions. The

Table 2. Comparisons Between Landsat and MODIS Water Surface Area Estimations

|	Hirakud	Nagarjuna Sagar	Pong	R. P. Sagar	Rengali
Landsat area (km^2)	572	185	207	160	189
MODIS area (km^2)	554	179	195	158	195
Total error (km^2)	−18	−6	−12	−2	6
Percent error[a] (%)	3	3	6	1	3

[a]Percent error is defined as |MODIS area—Landsat area|/Landsat area × 100%.

enhanced MODIS classification algorithm also showed good performance when some pixels of the original NDVI images were of low quality (i.e., the Nagarjuna Sagar, R. P. Sagar, and Pong reservoirs). For the Nagarjuna Sagar reservoirs, pixels in the black boxes would have been misclassified as "nonwater" if the enhancement operation was not performed. Noise in the Pong reservoir NDVI image was also effectively removed in final MODIS classification image. For the R. P. Sagar reservoir, there is an island within the region marked by a box in Figure 9. Due to the MODIS NDVI quality issue, the island in the original MODIS image is much smaller than that in Landsat. The underestimated island area was corrected in the enhancement operation by rectifying the misclassification using the historical percentile coverage information.

To evaluate the elevation and storage estimations, observation data were obtained from the CEA, (http://www.cea.nic.in/hyd_arch.html), which provides daily observed water storage (V_o) and water level (h_o) for 30 hydropower reservoirs (data available since 2008, with roughly a 2–4 month lag time). For comparison purposes, another remotely sensed data set was generated over these five reservoirs from the same data source (i.e., MODIS and ICESat/GLAS) using the algorithm by *Gao et al*. [2012]. Figure 10 shows the validation results of these two algorithms. Among the five reservoirs, both algorithms performed the best over the Hirakud. This is because the Hirakud has the largest area (among the five evaluated reservoirs) and it is surrounded by heavy vegetation whose NDVI values are very distinctive from those of water. For the Pong reservoir, *Gao et al*.'s [2012] algorithm tends to underestimate when the storage was large while overestimate when the reservoir was small. Examination of a series of MODIS classification images for this reservoir using both algorithms (results are not shown) suggest that the *Gao et al*. [2012] approach had overestimated the area when the reservoir was about half full. Since the *Gao et al*. [2012] approach created two classes (i.e., "water" and "nonwater"), the wetland was often misclassified as "water." But when the reservoir was mostly full or mostly empty, the wetland was either very small or had a great contrast to the water. A direct consequence of this is a skewed area-elevation relationship—which ultimately led to the elevation and storage errors. To overcome this problem, we designated three classes (with "wetland" as a standalone class) instead of two. For this particular reservoir, a large wetland was created when the water level retreated to its middle range.

According to the statistics in Table 3, the R^2 values between the remotely sensed results (elevation and storage) from this study and in situ data ranged from 0.83 to 0.96. The new algorithm outperformed the *Gao et al*. [2012] algorithm in all cases except for the elevation bias at Nagarjuna Sagar. Taking the NRMSE of
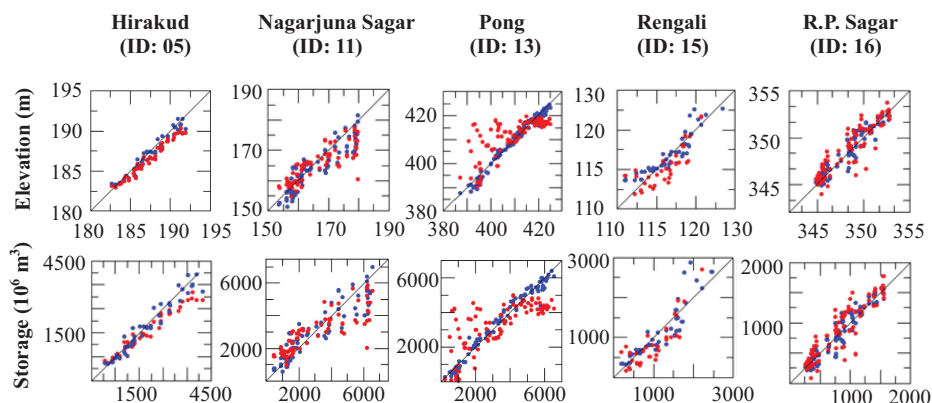
Figure 10. Validations of the remotely sensed water surface elevation and storage data using gauge observations (available since 2008, with 2–4 months lag) over five reservoirs. The *x* axis is the observation data and the *y* axis is the remotely sensed result. The blue dots represent results obtained from the enhanced algorithm in this paper and the red dots are results based on the *Gao et al*. [2012] algorithm.

Table 3. Statistical Validation Results for the Remotely Sensed Reservoir Elevation (h) and Storage (V)

		Hirakud		Nagajuna Sagar		Pong		Rengali		R. P. Sagar	
		Gao[a]	Zhang[b]	Gao	Zhang	Gao	Zhang	Gao	Zhang	Gao	Zhang
R^2	H	0.96	0.96	0.69	0.85	0.55	0.98	0.62	0.83	0.81	0.92
	V	0.92	0.94	0.69	0.85	0.56	0.98	0.71	0.85	0.81	0.92
Bias	h (m)	−0.84	−0.34	−1.20	−1.45	2.02	0.22	−0.47	0.33	0.42	0.22
	V (10^6 m^3)	−284.50	−98.10	−136.30	−32.30	138.69	10.70	−133.90	6.08	47.47	12.35
NRMSE	H (%)	11.28	7.43	10.61	6.78	28.32	6.45	16.27	12.68	6.87	4.45
	V (%)	18.87	12.77	36.52	24.75	37.77	9.51	43.60	25.20	24.21	15.45

[a]Gao refers to the algorithm in *Gao et al.* [2012].
[b]Zhang refers to the algorithm in this study.

storage as an example, this algorithm led to an improvement [over *Gao et al.*, 2012] of 6.10%, 11.77%, 28.26%, 18.40%, and 8.76% for the Hirakud, Nagarjuna Sagar, Pong, R. P. Sagar, and Rengali, respectively. This result suggests that both the calibrated reservoirs (Pong and Hirakud) and the uncalibrated reservoirs have been improved similarly. As explained in sections 3.1, the key differences between these two algorithms are the number of classes used in the *k*-mean unsupervised classification and the postclassification filtering procedure. The algorithm used in this study outperformed *Gao et al.* [2012] in both accounts. First, the generation of three classes meant that the misclassifications of the pixels along the shore were reduced. Second, the postclassification enhancement employed a more realistic weighted procedure that took into account that percentile zone a pixel belonged to (versus the simple "majority filter" method, which treats all pixels evenly across the entire classification image).

The results from Table 3 also suggest multicriteria should be considered for a comprehensive evaluation. Although a low correlation indicates low accuracy, a high correlation does not necessarily mean there is not a problem. For instance, the R^2 values from both algorithms are very high over the Hirakud, but the biases using the *Gao et al.* [2012] algorithm were much larger than those from our algorithm due to underestimations. Another example is the Nagarjuna Sagar reservoir. Although the bias of elevation at the Nagarjuna Sagar reservoir was smaller from the *Gao et al.* [2012] algorithm, the method proposed in this study performs better when R^2 and NRMSE are both considered.

4.2. Uncertainty Analysis

In this section, uncertainty analysis for the remotely sensed storage estimations was conducted. The sources of storage estimation error include ICESat/GLAS elevation error, MODIS water surface area error, area-elevation relationship error, and the reservoir configuration errors. Specifically, we investigated the uncertainty of storage associated with two sources: the surface area estimation and the ICESat/GLAS elevation data. The first part of the area-elevation relationship error, which is directly caused by these two sources, is therefore addressed implicitly. The second part of the area-elevation relationship error is related to the assumption of a linear area-elevation relationship. Although the real area-elevation relationship is most likely nonlinear and can vary if the slope changes, the error from the linear approximation is not due to a lack of information. The reservoir configuration errors are errors associated with the reported reservoir characteristics at capacity (storage, area, and elevation). When the reservoir configurations are biased, an offset with the remotely sensed storage will be created according to equation (4). However, the storage variation is not affected by this error source, since the constants at capacity will be canceled out when storage change is calculated. The other error sources, such as the fluvial sedimentation, may cause storage overestimation over time. Nonetheless, according to the storage time series in Figure 11, none of the 21 reservoirs has shown a clear increasing trend that can be related to a sedimentation effect over the 13 years. Because of the above reasons—and because the reservoir configuration and the sedimentation errors are hard to quantify—uncertainties due to these two sources are not discussed.

4.2.1. Uncertainty Due to Parameter Selection in Water Area Classification

During the water area classification process (as described in section 3), parameterization uncertainty is related to the selection of two parameters: C_P and C_Q. In equation (3), C_P is set to 0.7 based on "trial and error" over the Pong and Hirakud reservoirs. When Cp is set to a lower value (e.g., 0.5), a nonwater pixel will have a higher possibility to be assigned as water (according to equation (3)). In order to test the uncertainty of C_P, we calculated the storage difference between $C_P = 0.5$ and $C_P = 1$ for each of the 21 reservoirs. Figures 12a and 12b
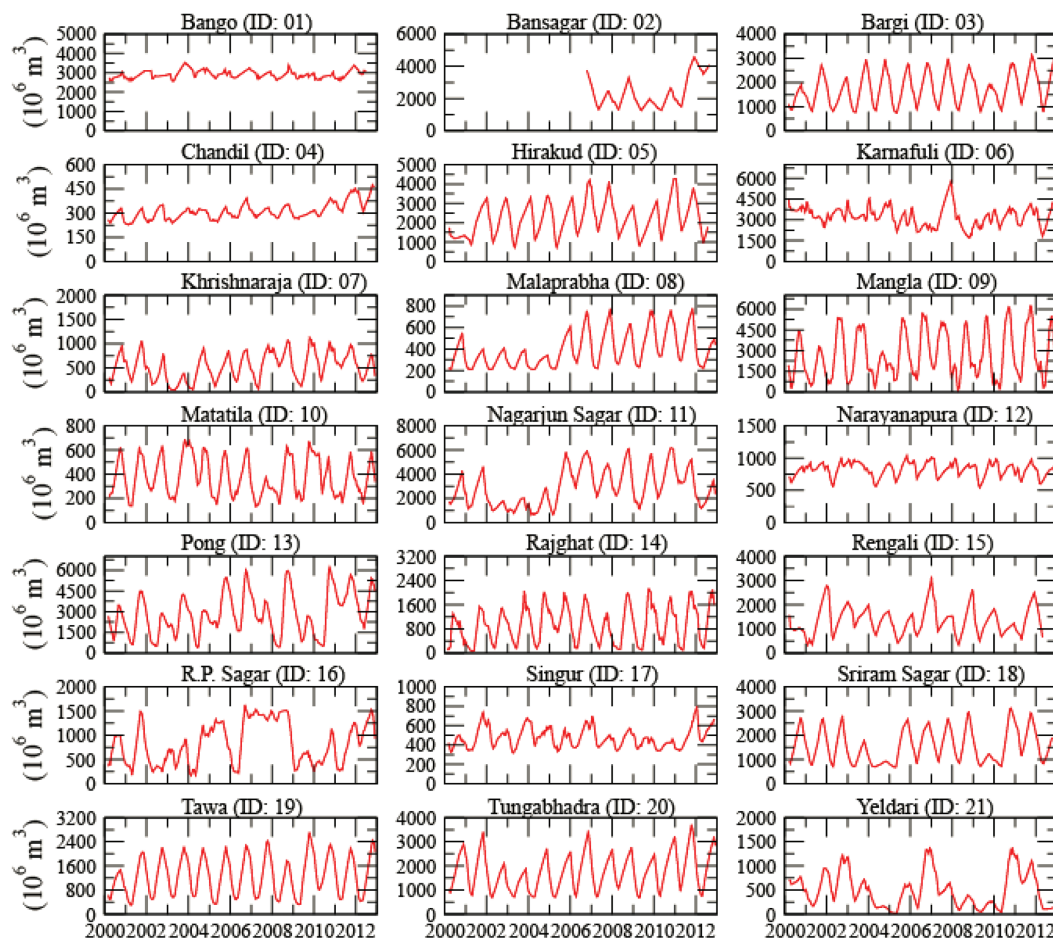
**Figure 11.** Remotely sensed storage time series for the 21 South Asian reservoirs.

show the absolute uncertainty and relative uncertainty due to the choice of C_p. The absolute uncertainty increases as the reservoir capacity increases, while the relative uncertainly has no clear relationship with the capacity. The average relative uncertainty is 5.54%. The second parameter, C_Q, is used as a criterion to identify whether a classification should be considered "good" or "poor." When C_Q is set to 0 (i.e., the minimum of Q), the final classification results (after the enhancement operation) for most of images will be similar to the results derived by the K-means algorithm, which tends to underestimate the water surface area. However, when C_Q is set to 0.25 (i.e., the maximum of Q), although noise can be easily deleted, the water surface area may be overestimated. The difference between the storage estimation values when using $C_Q = 0$ and $C_Q = 0.25$ represents the uncertainty of a given reservoir. The absolute uncertainty and relative uncertainty associated with C_Q for the 21 reservoirs are shown in Figures 12c and 12d, respectively. Although the absolute uncertainty due to C_Q shares a similar pattern with that due to C_p, the relative uncertainty due to C_Q converges to a small value (of 2–3%) as the reservoir size increases. Overall, the choice of C_p adds more uncertainty than the selection of C_Q. Nonetheless, these relative uncertainties are smaller than the NRMSE values in Table 3.

4.2.2. Uncertainty Due to ICESAT/GLAS Elevation

Each elevation data record that was used for the area-elevation relationship represented the average of all ICESat/GLAS observations over a given reservoir. Therefore, there is an uncertainty associated with this averaged elevation. This uncertainty could be from sensor measurement errors and/or natural variations (including surface roughness and surface wind). Equation (8) shows the uncertainty of storage due to elevation uncertainty:

$$\Delta V = (A_c + A_{RS})\Delta h/2 \qquad (8)$$

where ΔV is the storage uncertainty due to the ICESat/GLAS elevation, A_c is the reservoir area at capacity, and A_{RS} is the estimated area from MODIS. Δh is the difference between the maximum and minimum
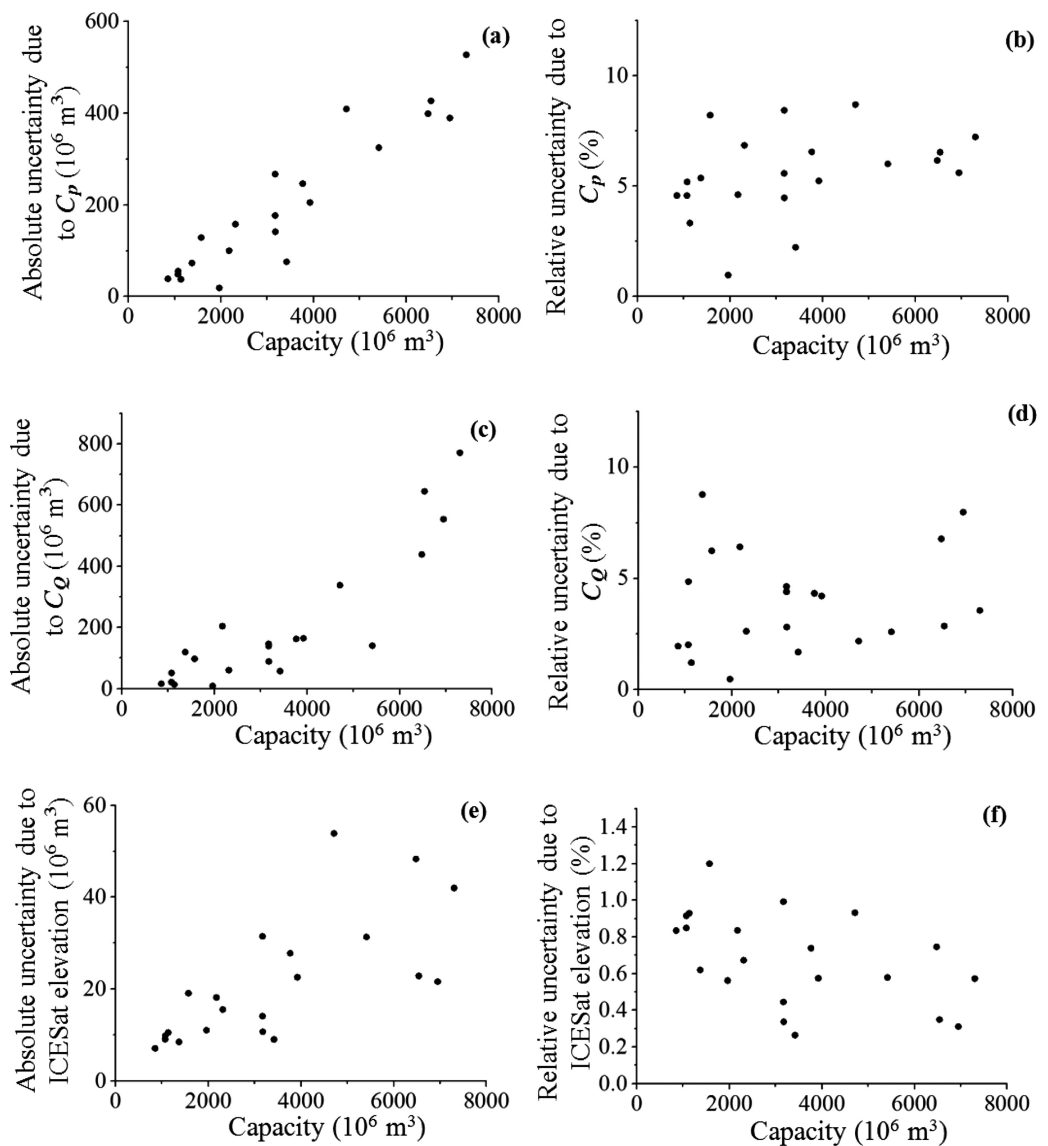
Figure 12. Uncertainty analysis results. (a) Absolute uncertainty due to C_p in water area classification; (b) relative uncertainty due to C_P in water area classification; (c) absolute uncertainty due to C_Q in water area classification; (d) relative uncertainty due to C_Q in water area classification; (e) absolute uncertainty due to ICESat elevation observations; and (f) relative uncertainty due to ICESat elevation observations.

ICESat/GLAS elevation values over the water surface along the track on the observation day. Unlike the quantification of uncertainties due to parameterization, the calculation of uncertainty due to elevation is based on analyzing real observations from ICESat/GLAS. Because of the relatively high accuracy of ICESat/GLAS elevation data (less than 10 cm according to *Zhang et al.* [2011]), uncertainty of storage caused by elevation is much smaller than that caused by area estimation. Although the absolute uncertainty in Figure 12e has a similar trend as those shown in Figures 12a and 12c, it is about an order of magnitude smaller. For relative uncertainty, there was no noticeable trend when the size of the reservoir changed. The relative uncertainty due to ICESat/GLAS elevation ranged from 0.34% to 1.67%, and its mean value was 0.67% (Figure 12f).

4.3. Reservoir Storage Variations in South Asia
Figure 11 shows the storage variations for the 21 studied reservoirs in South Asia from 2000 to 2012. The total capacity of theses reservoirs is 83.9 km³. The record length for all reservoirs is 13 years except for the

Bansagar reservoir (where construction was not completed until 2006). A few examples that explore the hydrological implications of these storage time series are as follows.

Built in 1975, the Pong reservoir (i.e., Maharana Pratap Sagar) is the highest earthfill dam in India. It is located on the Beas River within the wetland zone of the Siwalik Hills (i.e., the Outer Himalayas) in the state of Himachal Pradesh. Because it is close to Himachal Mountain, upstream snow and glacial melt contributes substantially to the lake inflows. With large temperature and precipitation variations, this region is prone to floods during the monsoon season. According to the Global Active Archive of Large Flood Events database [*Brakenridge et al.*, 2002], major floods in August of 2001 and 2007 caused 16 and 76 fatalities, respectively. These flood events are well represented by the peaks shown in the Pong reservoir storage time series in Figure 11. Also, in January 2010, the storage was only 20% of capacity, which reflects the 2009–2010 drought in the Himachal area.

Yeldari reservoir, another earthfill dam in India, is mainly used for irrigation and hydroelectricity generation. According to media reports, two severe drought events occurred in the region in 2004 and 2012, and the Yeldari dam reservoir almost dried up in both cases ("38 reservoirs down to 30 percent storage" from *Rediff Business*, http://www.rediff.com/money/report/water/20040728.htm, 2004; and "Marathwada remains parched" from the *Afternoon & Courier*, http://www.afternoondc.in/city-news/marathwada-remains-parched/article_65090, 2012). The remotely sensed storage of the Yeldari has demonstrated clear consistency with the reported results. Moreover, the satellite estimated time series indicates that the 2004 drought lasted until the beginning of 2005 and that there was another (smaller magnitude) drought in 2009.

Another example is the Bansagar reservoir, which is located on the Sone River and is used for irrigation and hydroelectricity generation. The dam construction was started in 1978 and completed in 2006. According to Figure 11, Bansagar reservoir water storage kept increasing in 2011 until the fall season. Following the sudden water release into the Sone river (from the reservoir) and the heavy rainfall in its downstream area, several villages in the Rohtas, Arwal, Patna, Aurangabad, and Bhojpur districts were reportedly inundated ("Flood alert sounded in Bihar" from *The Hindu*, http://www.thehindu.com/todays-paper/tp-national/tp-new-delhi/flood-alert-sounded-in-bihar/article2489034.ece, 2011, *media report*).

The upper drainage basin of the Mahanadi River is characterized by periodic droughts, which is a contrast to the lower delta region where floods are common. The Hirakud reservoir was constructed to help alleviate these problems by regulating river flows. The reservoir also produces hydroelectricity through several hydroelectric plants. In 2000, the region suffered from historic drought, which is effectively reflected by the low storage values (Figure 11). Although the reservoir storage is directly affected by inflows, the operation rules play an important role in regulating the storage. It was reported that Hirakud kept the water level higher than the recommended value in 2008. When inflows increased suddenly, the Hirakud released water (in order to protect the dam) which led to a man-made flood in the downstream area [*Choudhury et al.*, 2012]. Although 2009 and 2010 were two dry years, the Hirakud reservoir peak storage was maintained at about 70% of capacity. When heavy precipitation occurred in September 2011, the mismanagement of the Hirakud reservoir caused avoidable flooding [*Choudhury et al.*, 2012].

5. Summary and Conclusions

In this study, a remotely sensed reservoir data set in South Asia, which includes elevation, area, and storage information, was generated using a novel multisatellite algorithm. First, the MODIS-derived water classifications and ICESat/GLAS data (when available) were used to create an area-elevation relationship for each of the 21 selected reservoirs. Next, the elevation and storage variations were estimated over the period of 2000–2012 using the MODIS-based surface area time series and the area-elevation relationships. The ICESat/GLAS has a much higher spatial resolution (70 m) than the satellite radar altimetry data (several kilometers), which allows it to measure much smaller reservoirs. However, in the past, its short lifetime (2003–2010) and low repeat frequency (91 days) had limited the capability of ICESat/GLAS with regards to monitoring lakes and reservoirs. By combining MODIS and ICESat/GLAS for reservoir storage estimations, we were able to take the advantage of both satellites. Furthermore, this satellite-based reservoir data set was validated by both high-resolution Landsat ETM+ classifications and gauge observations over five locations. Last, we also conducted uncertainty analysis for the remotely sensed storage estimations. Specifically, we investigated the uncertainty of storage associated with two factors: the surface area

classification parameterizations and the ICESat/GLAS elevation measurements. The conclusions of this study are summarized as follows:

1. The postclassification image enhancement procedure significantly improved the MODIS water area estimation accuracy, which is essential for the area driven (versus elevation driven) storage estimation algorithm used in this study.
2. By using MODIS area estimations and ICESat elevations to derive the reservoir area-elevation relationship, the retrieval algorithm developed in this study has the potential to be applied to other regions where reservoir storage information is hard to acquire and radar altimetry observations are few.
3. Uncertainty analysis results suggest that the uncertainties associated with the area algorithm parameter selections are larger than those due to elevation measurements. Nonetheless, the uncertainties are less than 10% in all cases.
4. Considering the abundance of transboundary rivers in this region, this reservoir storage data set can serve as a valuable data source for water resources management purposes, such as hydropower generation, irrigation water supply allocations, and disaster mitigations. By incorporating remotely sensed reservoir storage information into hydrological modeling, better model prediction skills are expected (false alarms can be avoided).
5. The remote sensing-based reservoir storage estimation algorithm from this study is general and transferable to global applications for lakes and reservoirs. The data set can be used for improving the representation of water resources management in Earth System Modeling, for incorporating lakes into weather forecasting models and climate models, and for addressing human interferences to regional hydrologic processes.

Although this storage data set represent 28% of the integrated reservoir capacity in South Asia—which is first of its kind to the best of our knowledge—observations over more reservoirs would be highly valuable for this region (with its dense river networks). Unfortunately, due to the relatively sparse orbital coverage of ICESat/GLAS and the relatively coarse spatial resolution of MODIS, the reservoirs were limited to what was presented by this study. With the launch of the ICESat2 mission in 2016 and the Surface Water and Ocean Topography (SWOT) mission in 2019, both of which feature higher-resolution altimeters, a significantly greater number of reservoirs will be able to be studied over an extended time period (beginning when MODIS data was first available) using the techniques developed in this study.

References

Adhikari, P., Y. Hong, K. R. Douglas, D. B. Kirschbaum, J. Gourley, R. Adler, and B. G. Robert (2010), A digitized global flood inventory (1998–2008): Compilation and preliminary results, *Nat. Hazards*, 55(2), 405–422, doi:10.1007/s11069-010-9537-2.

Al-amri, S. S., N. V. Kalyankar, and S. D. Khamitkar (2010), A comparative study of removal noise from remote sensing image, *IJCSI Int. J. Comput. Sci. Issues*, 7(1), 32–36.

Biancamaria, S., F. Hossain, and D. Lettenmaier (2011), Forecasting transboundary river water elevations from space, *Geophys. Res. Lett.*, 38, L11401, doi:10.1029/2011GL047290.

Birkett, C. M. (1998), Contribution of the TOPEX NASA radar altimeter to the global monitoring of large rivers and wetlands, *Water Resour. Res.*, 34(5), 1223–1239, doi:10.1029/98WR00124.

Birkett, C. M., and B. Beckley (2010), Investigating the performance of the Jason-2/OSTM radar altimeter over lakes and reservoirs, *Mar. Geod.*, 33(S1), 204–238, doi:10.1080/01490419.2010.488983.

Boser, B. E., I. M. Guyon, and V. N. Vapnik (1992), A training algorithm for optimal margin classifiers, in *Proceedings of 5th Annual ACM Workshop on Computer Learning Theory*, pp. 144–152, ACM New York, N. Y., doi:10.1145/130385.130401.

Brakenridge, R., S. Caquard, E. Anderson, and H. Carlos (2002), Potential uses of space-base flood mapping for disaster management in Asia and the Pacific, paper presented at UN Regional Workshop on Space Technology, Bangkok. [Available at http://www.unoosa.org/oosa/en/SAP/sched/2002.html.]

Bulygina, N., and H. Gupta (2011), Correcting the mathematical structure of a hydrological model via Bayesian data assimilation, *Water Resour. Res.*, 47, W05514, doi:10.1029/2010WR009614.

Calmant, S., F. Seyler, and J. F. Cretaux (2008), Monitoring continental surface waters by satellite altimetry, *Surv. Geophys.*, 29, 247–269, doi:10.1007/s10712-008-9051-1.

Cheema, M., and W. Bastiaanssen (2010), Land use and land cover classification in the irrigated Indus Basin using growth phenology information from satellite data to support water management analysis, *Agric. Water Manage.*, 97(10), 1541–1552, doi:10.1016/j.agwat.2010.05.009.

Choudhury, P., J. Sandbhor, and P. Satapathy (2012), Floods, fields and factories: Towards resolving conflicts around the Hirakud Dam, action research report, Forum for Policy Dialogue on Water Conflicts in India. [Available at http://www.academia.edu/1993991/Floods_Fields_and_Factories_Towards_Resolving_Conflicts_around_the_Hirakud_Dam.]

Cortes, C., and V. N. Vapnik (1995), Support vector networks, *Mach. Learning*, 20, 273–297.

Crétaux, J.-F., W. Jelinski, S. Calmant, A. Kouraev, V. Vuglinski, M. Bergé-Nguyen, M.-C., Gennero, F. Nino, R. Abarca Del Rio, and A. Cazenave (2011), SOLS: A lake database to monitor in the Near Real Time water level and storage variations from remote sensing data, *Adv. Space Res.*, 47(9), 1497–1507, doi:10.1016/j.asr.2011.01.004.

Dewidar, K. M. (2011), Monitoring temporal changes of the surface water area of the Burullus and Manzala lagoons using automatic techniques applied to a Landsat satellite data series of the Nile Delta coast, *Mediter. Mar. Sci.*, *12*(2), 462–478, doi:10.12681/mms.45.

Duan, Z., and W. G. M. Bastiaanssen (2013), Estimating water volume variations in lakes and reservoirs from four operational satellite altimetry databases and satellite imagery data, *Remote Sens. Environ.*, *134*, 403–416, doi:10.1016/j.rse.2013.03.010.

Duda, R. O., P. E. Hart, and D. G. Stock (2001), *Pattern Classification Second Edition*, John Wiley, N. Y.

Gao, H., C. Birkett, and D. P. Lettenmaier (2012), Global monitoring of large reservoir storage from satellite remote sensing, *Water Resour. Res.*, *48*, W09504, doi:10.1029/2012WR012063.

Gonzalez, R. C., and R. E. Woods (2007), *Digital Image Processing*, Pearson Prenctice Hall, N. J.

Huffman, G. J., D. T. Bolvin, E. J. Nelkin, D. B. Wolff, R. F. Adler, G. Gu, Y. Hong, K. P. Bowman, and E. F. Stocker (2007), The TRMM multisatellite precipitation analysis (TMPA): Quasi-global, multiyear, combined-sensor precipitation estimates at fine scales, *J. Hydrometeorol.*, *8*(1), 38–55, doi:10.1175/JHM560.1.

Islam, A., S. Bala, and M. Haque (2010), Flood inundation map of Bangladesh using MODIS time-series images, *J. Flood Risk Manage.*, *3*(3), 210–222, doi:10.1111/j.1753-318X.2010.01074.x.

Jain, A. K. (2010), Data clustering: 50 years beyond *K*-means, *Pattern Recognition Lett.*, *31*(8), 651–666, doi:10.1016/j.patrec.2009.09.011.

Ji, L., L. Zhang, and B. Wylie (2009), Analysis of dynamic thresholds for the normalized difference water index, *Photogramm. Eng. Remote Sens.*, *75*(11), 1307–1317.

Lehner, B., C. R. Liermann, C. Revenga, C. Vörösmarty, B. Fekete, P. Crouzet, P. Döll, M. Endejan, K. Frenken, and J. Magome (2011), High-resolution mapping of the world's reservoirs and dams for sustainable river-flow management, *Frontiers Ecol. Environ.*, *9*(9), 494–502, doi:10.1890/100125.

Li, J., H. Fang, and L. Yang (2011), Mapping lake level changes using ICESat/GLAS satellite laser altimetry data–A case study in arid regions of central Asia, in *MIPPR 2011: Remote Sensing Image Processing, Geographic Information Systems, and Other Applications, Procceings of SPIE*, 80060J, SPIE, Guilin, China.

Lu, S., B. Wu, N. Yan, and H. Wang (2011), Water body mapping method with HJ-1A/B satellite imagery, *Int. J. Appl. Earth Obs. Geoinf.*, *13*(3), 428–434, doi:10.1016/j.jag.2010.09.006.

Maulik, U., and I. Saha (2010), Automatic fuzzy clustering using modified differential evolution for image classification, *IEEE Trans. Geosci. Remote Sens.*, *48*(9), 3503–3510, doi:10.1109/TGRS.2010.2047020.

McKellip, R., B. Beckley, C. B. S. Birkett, B. Doorn, B. Grant, L. Estep, R. Moore, K. Morris, K. Ross, and G. Terrie (2004), *PECAD's Global Reservoir and Lake Monitor: A Systems Engineering Report*, Version 1.0, NASA/John C. Stennis Space Cent., Bay St. Louis, Miss.

Mercury, M., R. Green, S. Hook, B. Oaida, W. Wu, A. Gunderson, and M. Chodas (2012), Global cloud cover for assessment of optical satellite observation opportunities: A HysplRI case study, *Remote Sens. Environ.*, *126*, 62–71, doi:10.1016/j.rse.2012.08.007.

Phan, V. H., R. Lindenbergh, and M. Menenti (2012), ICESat derived elevation changes of Tibetan lakes between 2003 and 2009, *Int. J. Appl. Earth Obs. Geoinf.*, *17*, 12–22, doi:10.1016/j.jag.2011.09.015.

Rodrigues, L. N., E. E. Sano, T. S. Steenhuis, and D. P. Passo (2012), Estimation of small reservoir storage capacities with remote sensing in the Brazilian Savannah Region, *Water Resour. Manage.*, *26*(4), 873–882, doi:10.1007/s11269-011-9941-8.

Schutz, B., H. Zwally, C. Shuman, D. Hancock, and J. DiMarzio (2005), Overview of the ICESat mission, *Geophys. Res. Lett.*, *32*, L21S01, doi:10.1029/2005GL024009.

Shuman, C., H. Zwally, B. Schutz, A. Brenner, J. DiMarzio, V. Suchdeo, and H. Fricker (2006), ICESat Antarctic elevation data: Preliminary precision and accuracy assessment, *Geophys. Res. Lett.*, *33*, L07501, doi:10.1029/2005GL025227.

Solano, R., K. Didan, A. Jacobson, and A. Huete (2010), *MODIS Vegetation Index User's Guide (MOD13 Series), The Univ. of Ariz*, Tucson, Ariz.

Song, C., B. Huang, and L. Ke (2013), Modeling and analysis of lake water storage changes on the Tibetan Plateau using multi-mission satellite data, *Remote Sens. Environ.*, *135*, 25–35, doi:10.1016/j.rse.2013.03.013.

Wang, X., P. Gong, Y. Zhao, Y. Xu, X. Cheng, Z. Niu, Z. Luo, H. Huang, F. Sun, and X. Li (2013), Water-level changes in China's large lakes determined from ICESat/GLAS data, *Remote Sens. Environ.*, *132*, 131–144, doi:10.1016/j.rse.2013.01.005.

Wolf, A. T., J. A. Natharius, J. J. Danielson, B. S. Ward, and J. K. Pender (1999), International river basins of the world, *Int. J. Water Resour. Dev.*, *15*(4), 387–427, doi:10.1080/07900629948682.

Wu, G., and Y. Liu (2014), Satellite-based detection of water surface variation in China's largest freshwater lake in response to hydro-climatic drought, *Int. J. Remote Sens.*, *35*(11-12), 4544–4558, doi:10.1080/01431161.2014.916444.

Wu, H., R. F. Adler, Y. Hong, Y. Tian, and F. Policelli (2012), Evaluation of global flood detection using satellite-based rainfall and a hydrologic model, *J. Hydrometeorol.*, *13*(4), 1268–1284, doi:10.1175/JHM-D-11-087.1.

Xu, H. (2006), Modification of normalised difference water index (NDWI) to enhance open water features in remotely sensed imagery, *Int. J. Remote Sens.*, *27*(14), 3025–3033, doi:10.1080/01431160600589179.

Zaitchik, B. F., M. Rodell, and R. H. Reichle (2008), Assimilation of GRACE terrestrial water storage data into a land surface model: Results for the Mississippi River Basin, *J. Hydrometeorol.*, *9*, 535–548, doi:10.1175/2007JHM951.1.

Zhang, G., H. Xie, S. Kang, D. Yi, and S. F. Ackley (2011), Monitoring lake level changes on the Tibetan Plateau using ICESat altimetry data (2003–2009), *Remote Sens. Environ.*, *115*(7), 1733–1742, doi:10.1016/j.rse.2011.03.005.

Zwally, H., B. Schutz, W. Abdalati, J. Abshire, C. Bentley, A. Brenner, J. Bufton, J. Dezio, D. Hancock, and D. Harding (2002), ICESat's laser measurements of polar ice, atmosphere, ocean, and land, *J. Geodyn.*, *34*(3-4), 405–445, doi:10.1016/S0264-3707(02)00042-X.

Zwally, H. J., D. Yi, R. Kwok, and Y. Zhao (2008), ICESat measurements of sea ice freeboard and estimates of sea ice thickness in the Weddell Sea, *J. Geophys. Res.*, *113*, C02S15, doi:10.1029/2007JC004284.